

**ESI for**

**Utilisation of carbon dioxide and nitrate for urea  
electrosynthesis with a Cu-based metal-organic framework**

Meng-Di Zhang,<sup>#a</sup> Jia-Run Huang,<sup>#a</sup> Pei-Qin Liao<sup>\*a</sup> and Xiao-Ming Chen<sup>\*ab</sup>

<sup>a</sup>MOE Key Laboratory of Bioinorganic and Synthetic Chemistry, GBRCE for Functional Molecular Engineering, School of Chemistry, IGCME, Sun Yat-Sen University, Guangzhou 510275, China.

<sup>b</sup>Chemistry and Chemical Engineering Guangdong Laboratory, Shantou 515031, China.

<sup>#</sup>These authors contributed equally.

E-mail: [liaopq3@mail.sysu.edu.cn](mailto:liaopq3@mail.sysu.edu.cn); [cxm@mail.sysu.edu.cn](mailto:cxm@mail.sysu.edu.cn)

## Supplementary Index

**Figure S1.**  $^1\text{H}$  NMR spectrum of HATNA-6OH.

**Figure S2.** SEM images of Cu-HATNA.

**Figure S3.** EDX profile of Cu-HATNA.

**Figure S4.** AC-TEM, HHADF image and the corresponding elemental mappings of Cu-HATNA.

**Figure S5.** Survey XPS spectrum of Cu-HATNA.

**Figure S6.** High-resolution Cu 2*p* XPS spectrum of Cu-HATNA.

**Figure S7.** Cu LMM Auger spectrum of Cu-HATNA.

**Figure S8.** TGA curve of Cu-HATNA.

**Figure S9.** LSV curves of Cu-HATNA in 0.1 M  $\text{KHCO}_3$  + 0.1 M  $\text{KNO}_3$  electrolyte.

**Figure S10.** Chronoamperometric curves at different potentials in 0.1 M  $\text{KHCO}_3$  + 0.1 M  $\text{KNO}_3$  electrolyte.

**Figure S11.** UV-vis absorption spectra of various urea concentrations and the calibration curve used for quantifying urea.

**Figure S12.** UV-vis absorption spectra of the electrolyte (0.1 M  $\text{KHCO}_3$  + 0.1 M  $\text{KNO}_3$ ) at different potentials.

**Figure S13.** Stability tests of Cu-HATNA at  $-0.5$  V vs RHE.

**Figure S14.** SEM images of Cu-HATNA after electrocatalysis.

**Figure S15.** AC-TEM images of Cu-HATNA after electrocatalysis.

**Figure S16.** PXRD patterns of Cu-HATNA before and after electrocatalysis.

**Figure S17.** High-resolution Cu 2*p* XPS spectrum of Cu-HATNA after electrocatalysis.

**Figure S18.** Cu LMM Auger spectrum of Cu-HATNA after electrocatalysis.

**Figure S19.** The background and baseline spectra of ATR-FTIR measurement.

**Figure S20.** Free energy diagram for  $\text{CO}_2\text{RR}$  and  $\text{NO}_3\text{RR}$  on Cu-HATNA.

**Table S1.** Comparison of electrocatalytic performance of Cu-HATNA toward urea synthesis with previously reported catalysts.

**Table S2.** Cu *K*-edge EXAFS curve Fitting Parameters.

## Experimental details

**Materials and general methods:** All reagents and chemicals were commercially available and without further purification. Ethylenediamine (EDA, >99%) and potassium nitrate ( $\text{KNO}_3$ , 99%) was purchased from Shanghai Aladdin Biochemical Technology Co., Ltd. Copper nitrate hemipentahydrate ( $\text{Cu}(\text{NO}_3)_2 \cdot 2.5\text{H}_2\text{O}$ , 98%) was purchased from Shanghai Macklin Biochemical Co., Ltd. Diquinoxalino[2,3-*a*:2',3'-*c*]phenazine-2,3,8,9,14,15-hexol (HATNA-6OH, >95%) was purchased from Chinese Academy of Sciences Yanshen Technology Co., Ltd. Potassium bicarbonate ( $\text{KHCO}_3$ , AR) was purchased from Guangdong Guanghua Sci-Tech Co., Ltd. Nafion (5 wt%, Dupont) and gas diffusion layer (GDL, CeTech GDL210S) were purchased from the corresponding reagent companies. All aqueous solutions were prepared with ultrapure water.

Powder X-ray diffraction (PXRD) data were recorded on a Miniflex-600 diffractometer (Cu  $K\alpha$ ). Scanning electron microscopy (SEM) images were obtained from a field emission scanning electron microscope (SU8010). Spherical aberration corrected transmission electron microscopy (AC-TEM) images were recorded by a JEM-ARM200P. X-ray photoelectron spectroscopy (XPS) measurements were conducted on an ESCALAB 250 spectrometer. The content of Cu in **Cu-HATNA** was measured by inductively coupled plasma atomic emission spectroscopy (ICP-AES) on a PerkinElmer Optima8300. Thermogravimetry analysis (TGA) was performed on a TGA55 analyser under  $\text{N}_2$  flow at a heating rate of  $10\text{ }^\circ\text{C min}^{-1}$ .

**X-ray absorption spectral measurement and data analysis:** The X-ray absorption spectra (XAS) including X-ray absorption near-edge structure (XANES) and extended X-ray absorption fine structure (EXAFS) of the samples at Cu (8979 eV) were collected at BL14W1 station in Shanghai Synchrotron Radiation Facility (SSRF), China. The Cu *K*-edge XANES data were recorded in a transmission mode. Cu foil,  $\text{Cu}_2\text{O}$  and CuO were used as reference, respectively. The acquired EXAFS data were extracted and processed according to the standard procedures using the ATHENA module implemented in the FEFFIT software packages.

**Attenuated total reflectance Fourier transform infrared spectroscopy (ATR-FTIR) measurements:** ATR-FTIR measurements were carried out on a Thermo Scientific Nicolet iS50 (Thermo Fisher) device. The Ge ATR crystal is placed in a three-electrode electrochemical cell. During ATR-FTIR measurements, Pt wire served as the counter electrode and the Ag/AgCl electrode served as the reference electrode. Data were collected after electrolysis for 10 min at

each potential from  $-0.3$  to  $-0.6$  V vs RHE. The collected background has been subtracted in all infrared spectra.

**Synthesis of Cu-HATNA:** Cu-HATNA was synthesised according to the literature.<sup>1</sup> HATNA-6OH (26.4 mg, 0.055 mmol) and  $\text{Cu}(\text{NO}_3)_2 \cdot 2.5\text{H}_2\text{O}$  (19.2 mg, 0.083 mmol) was dissolved in deionised water (5 mL) after 10 min of ultrasound. EDA (74  $\mu\text{L}$ ) was then added, the resulting mixture was sonicated for another 10 min and heated at  $85^\circ\text{C}$  for 2 days. Upon cooling, the black solid was collected by filtration and washed three times with DMF, water and acetone respectively.

**Preparation of working electrode:** The cathode gas diffusion electrodes (GDEs) were prepared by drop coating the catalyst ink over a GDL. 5 mg of electrocatalyst was dispersed in 1 mL of mixture isopropanol and 50  $\mu\text{L}$  of Nafion (5 wt% aqueous solution) with sonication for 60 min to form a homogenous ink. Then, 80  $\mu\text{L}$  of aforementioned ink was loaded onto the GDL and dried naturally to get working electrode. The geometric area of working electrode was  $1.0 \times 0.2 \text{ cm}^2$ , and the catalyst loading was  $\sim 1 \text{ mg cm}^{-2}$ .

**Electrochemical measurements:** All electrochemical measurements were carried out in the flow cell with a three-electrode system on a CHI660E electrochemical station. The pretreated anion exchange membrane (Dupont) acts as the separator. 0.1 M  $\text{KHCO}_3$  with 0.1 M  $\text{KNO}_3$  was employed as the electrolyte circularly supplied to the cathode and anode chambers through a peristaltic pump. Ag/AgCl electrode and a platinum plate were used as reference electrode and counter electrode, respectively. The  $\text{CO}_2$  flow rate was set to  $30 \text{ mL min}^{-1}$  during the electrocatalytic process. The applied potentials were measured against the Ag/AgCl reference electrode and converted to the RHE reference scale by  $E(\text{vs RHE}) = E(\text{vs Ag/AgCl}) + 0.197 \text{ V} + 0.059 \times \text{pH}$ .

**Product quantification:** As-produced urea was spectrophotometrically determined by diacetyl monoxime method.<sup>2</sup> First, 1 mL of electrolyte was removed from the cathodic chamber in turn. Then 2 mL of acid-ferric solution (100 mL of concentrated phosphoric acid, 300 mL of concentrated sulfuric acid, 600 mL of deionised water and 100 mg of ferric chloride) and 1 mL of diacetyl monoxime (DAMO)-thiosemicarbazide (TSC) solution (5 g of DAMO and 100 mg of TSC were dissolved in 1 L deionised water) were added. The resulting mixture was heated at  $90^\circ\text{C}$

°C for 30 min. After cooling to room temperature, the absorbance was acquired at 525 nm using a UV-vis spectrophotometer (UV-3600). The concentration–absorbance curves were calibrated using standard urea solutions, as shown in Figure S11, which contained the same concentrations of electrolytes as used in the electrocatalysis experiments.

The Faradaic efficiency (FE, %) is the ratio of the number of electrons transferred for the formation of urea to the total amount of electricity that flows through the circuit. Assuming sixteen electrons were needed to form one urea molecule, the FE and yield rate for urea synthesis could be calculated as follows:

$$FE_{urea} = \frac{16 \times F \times C_{urea} \times V}{60.06 \times Q} \times 100$$

$$Urea\ yield\ rate = \frac{C_{urea} \times V}{t \times m_{cat.}}$$

in which,  $F$  represents the Faraday constant (96485 C mol<sup>-1</sup>),  $Q$  represents the electric quantity,  $C_{urea}$  (ppm) represents the measured urea concentration,  $V$  (L) represents the volume of the electrolyte,  $t$  (h) represents the reduction time and  $m_{cat.}$  (g) represents the catalyst loadings.

**Computational details:** Density functional theory (DFT) calculations were performed using the Quantum Espresso (QE) software<sup>3-4</sup>. The revised Perdew-Bueke-Ernzerhof (RPBE) functional was used to describe exchange-correlation effects of electrons. We have chosen the projected augmented wave (PAW) potentials<sup>5</sup> to describe the ionic cores and take valence electrons into account using a plane wave basis set with an energy cut-off of 400 eV in all relaxation processes. The convergence criteria were set to 10<sup>-5</sup> eV for the energy and -0.03 eV/Å for the force. The k-point meshes were set of 2 × 2 × 1 for geometry optimization and electronic self-consistent.

## Supporting Figures

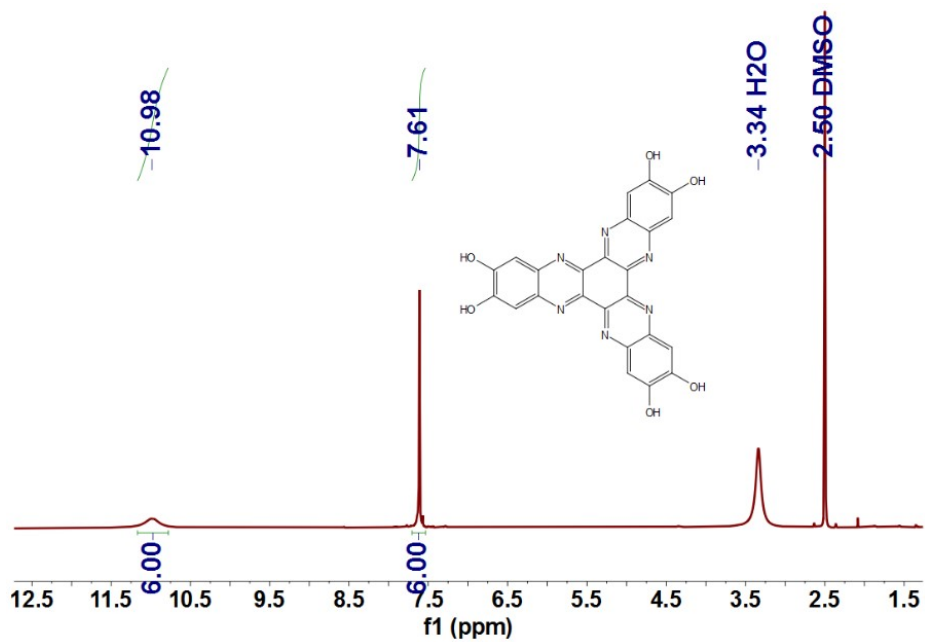


**Figure S1.**  $^1\text{H}$  NMR spectrum of HATNA-6OH.

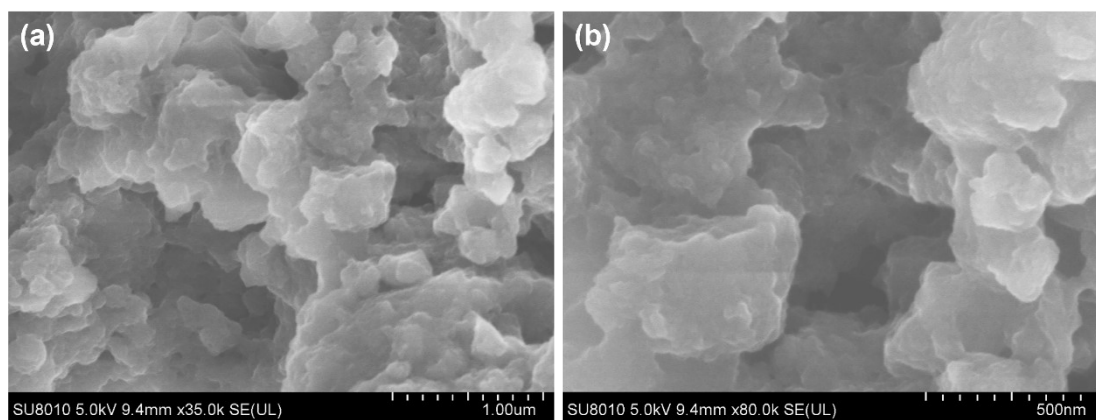


**Figure S2.** SEM images of Cu-HATNA at various magnifications.

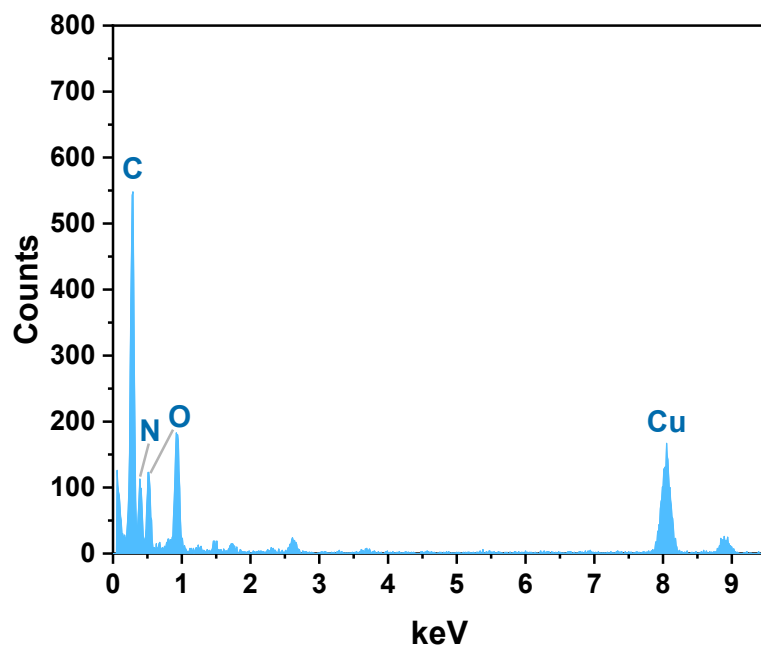


**Figure S3.** EDX profile of Cu-HATNA.

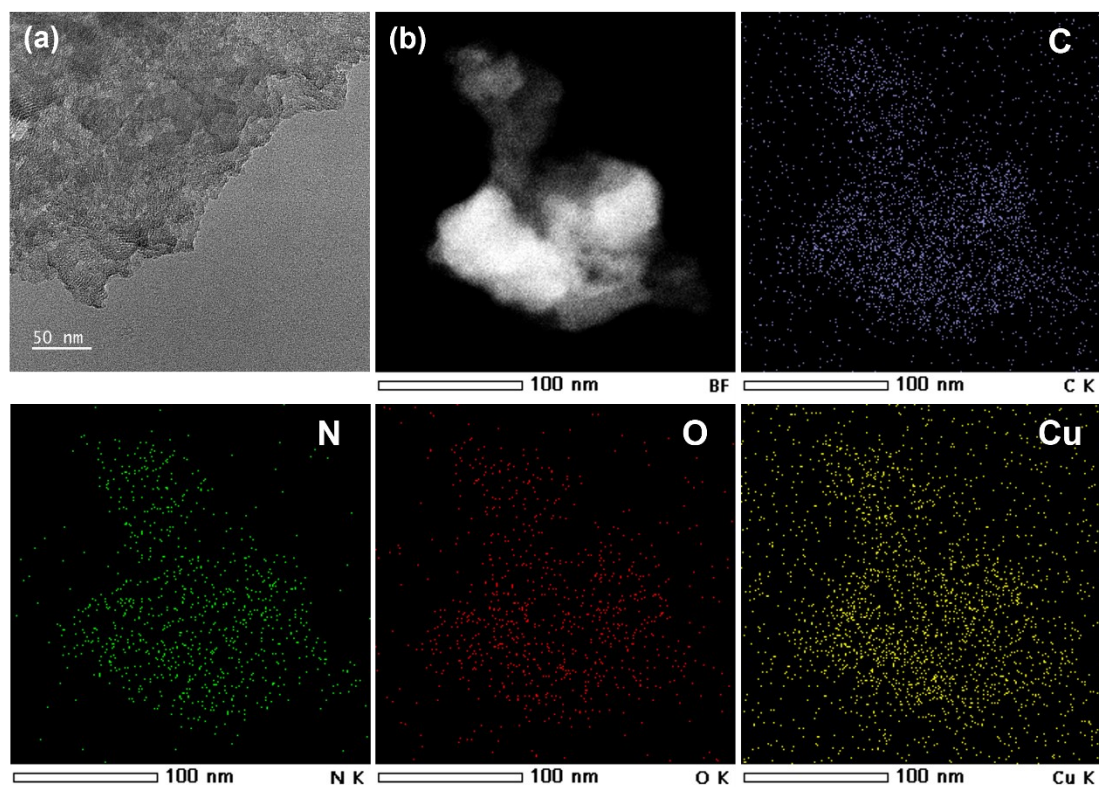


**Figure S4.** (a) AC-TEM image of Cu-HATNA with 50 nm scale-bar. (b) HHADF image and the corresponding C, N, O and Cu elemental mappings of Cu-HATNA.

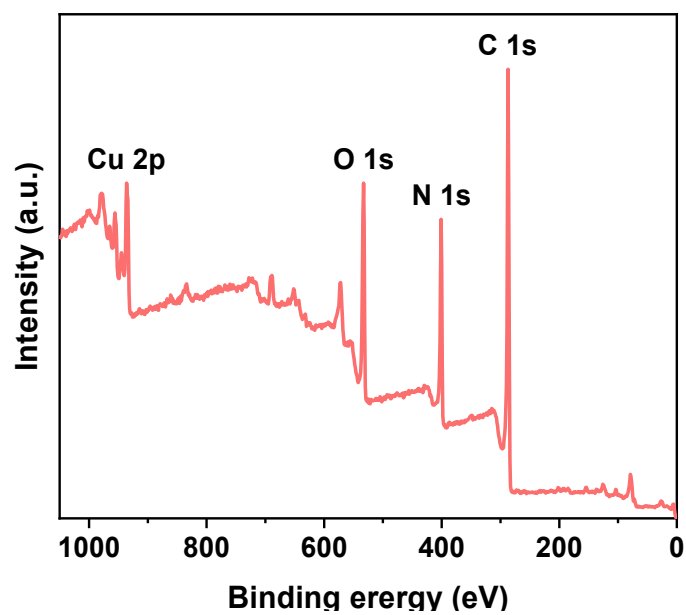


Figure S5. Survey XPS spectrum of Cu-HATNA.

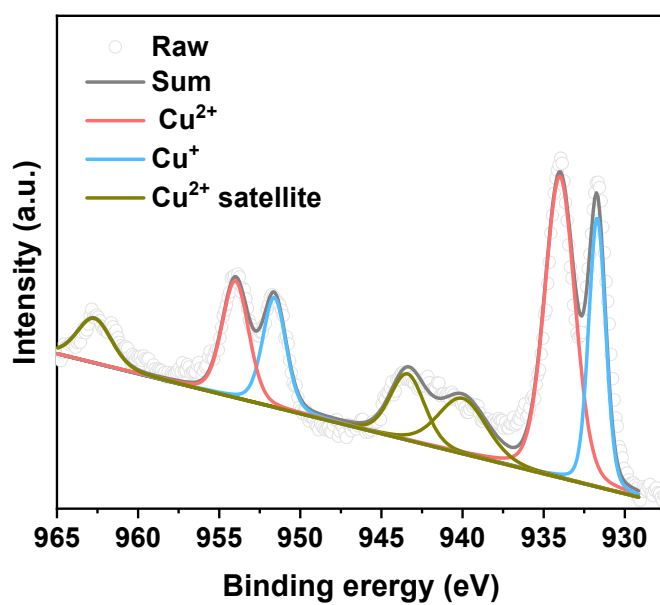
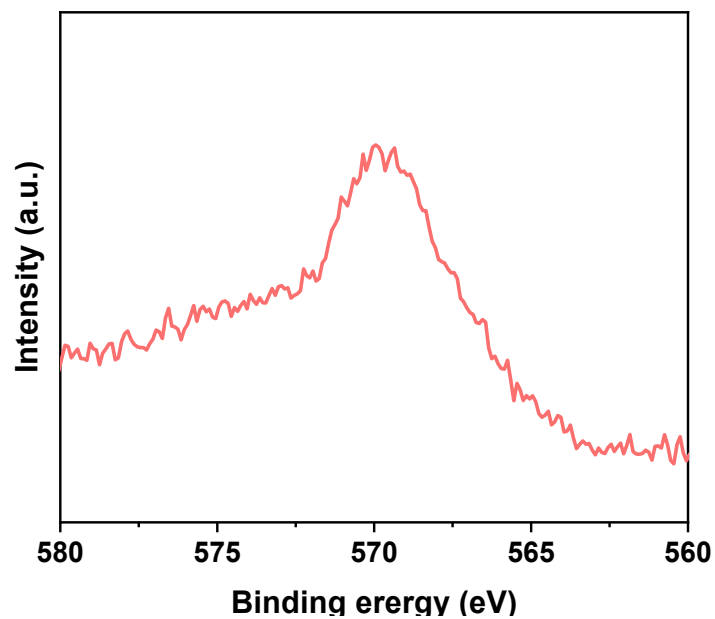
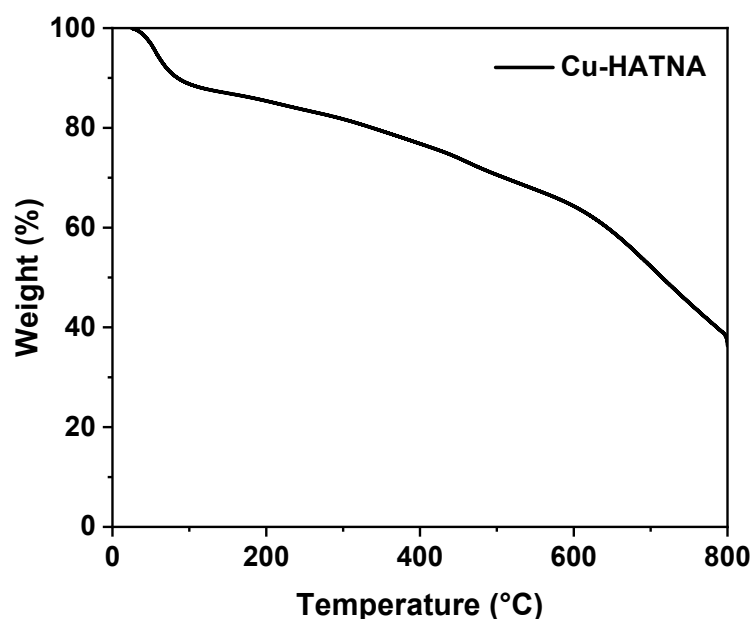


Figure S6. High-resolution Cu 2p XPS spectrum of Cu-HATNA.



**Figure S7.** Cu LMM Auger spectrum of Cu-HATNA.



**Figure S8.** TGA curve of Cu-HATNA measured under N<sub>2</sub> atmosphere with a heating rate of 10 °C min<sup>-1</sup>.

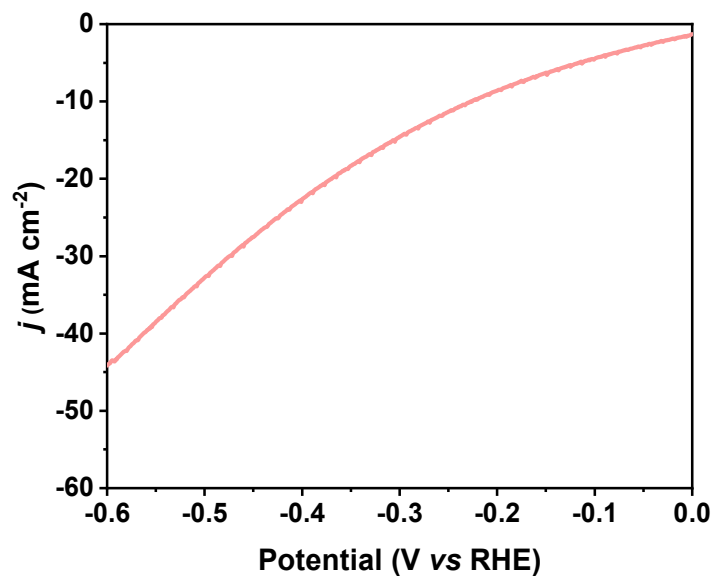


**Figure S9.** LSV curve of Cu-HATNA in 0.1 M KHCO<sub>3</sub> + 0.1 M KNO<sub>3</sub> electrolyte.

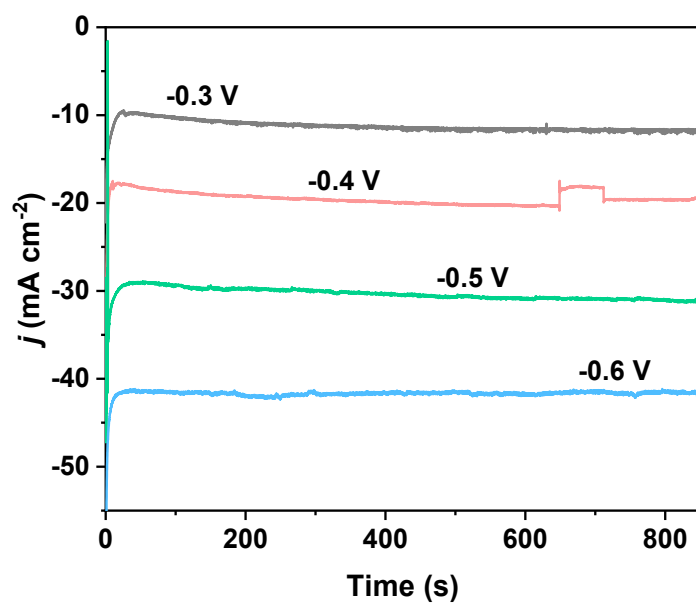


**Figure S10.** Chronoamperometric curves at different potentials in 0.1 M KHCO<sub>3</sub> + 0.1 M KNO<sub>3</sub> electrolyte.

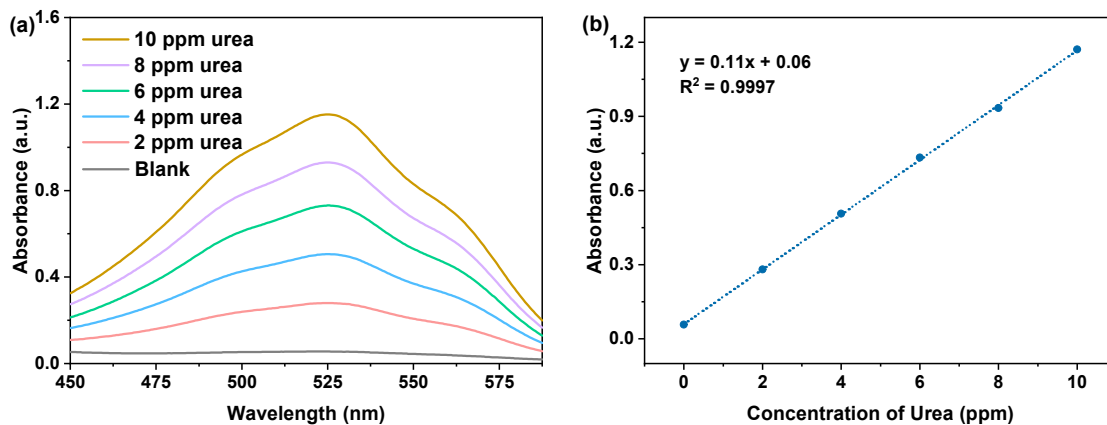


**Figure S11.** Diacetyl monoxime method for urea quantification. (a) UV-vis absorption spectra of various urea concentrations. (b) Calibration curve used for quantifying urea. The fitting curve shows good linear relation of absorbance with ammonia concentration ( $y = 0.11x + 0.06$ ,  $R^2 = 0.9997$ ) of three times independent calibration curves.

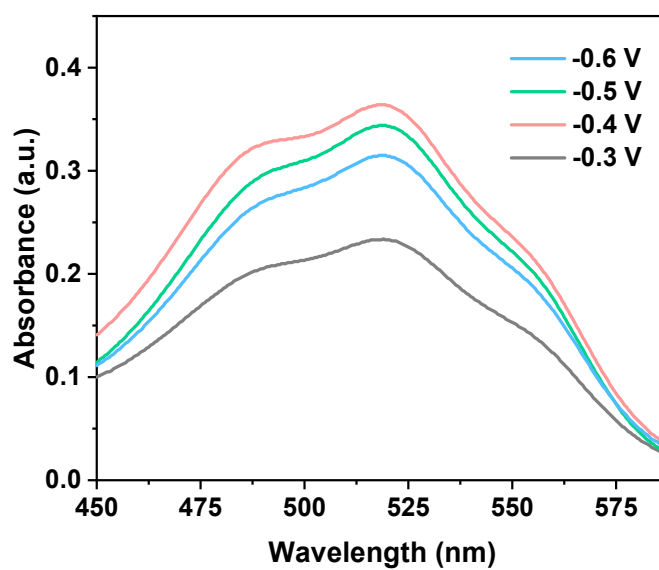


**Figure S12.** UV-vis absorption spectra of the electrolyte (0.1 M KHCO<sub>3</sub> + 0.1 M KNO<sub>3</sub>) at different potentials.

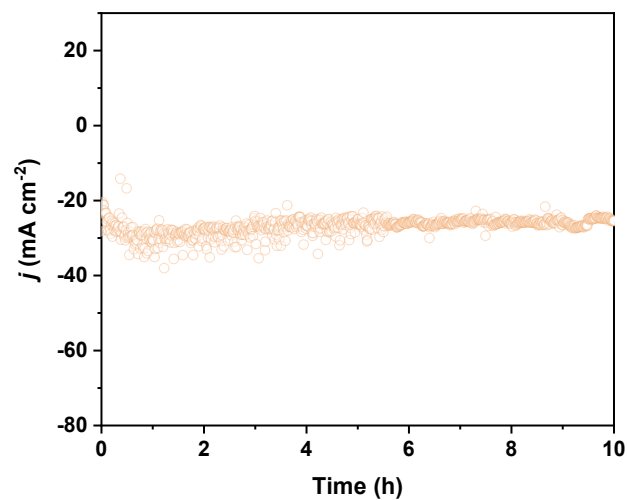


**Figure S13.** Stability tests of Cu-HATNA at  $-0.5$  V vs RHE.

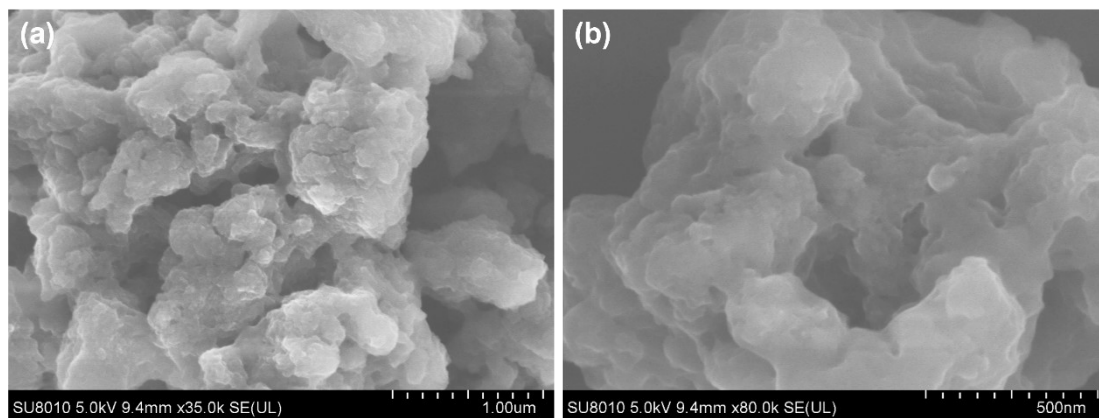


**Figure S14.** SEM images of Cu-HATNA after electrocatalysis.

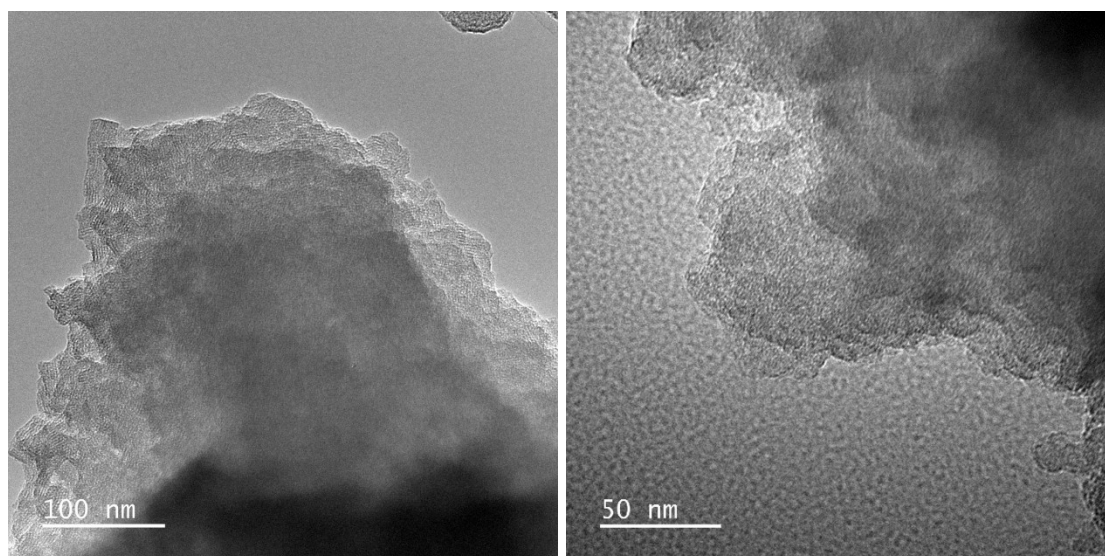


**Figure S15.** AC-TEM images of Cu-HATNA after electrocatalysis.

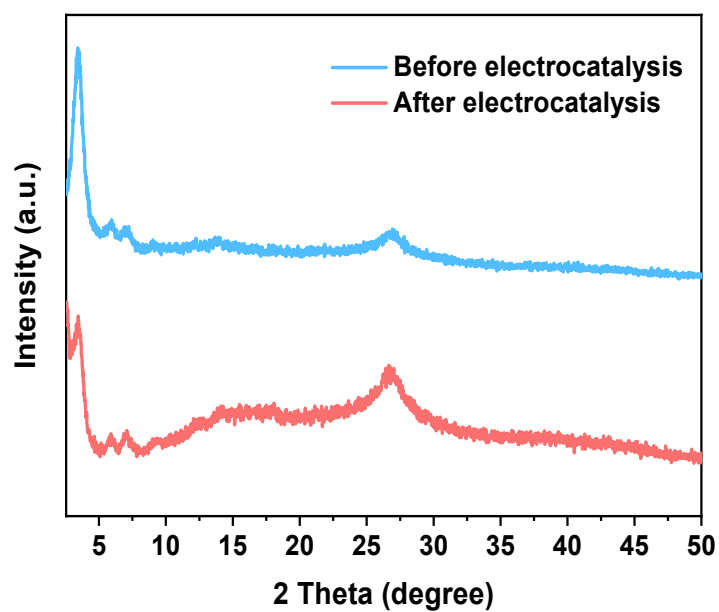


Figure S16. PXRD patterns of Cu-HATNA before and after electrocatalysis.

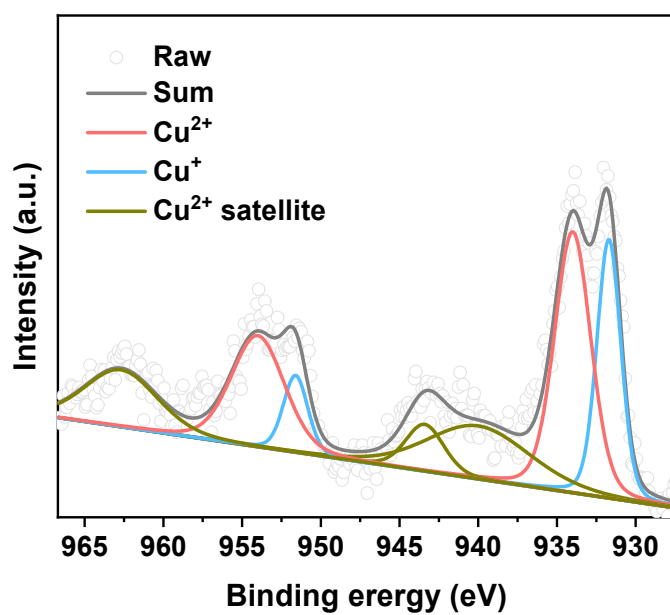
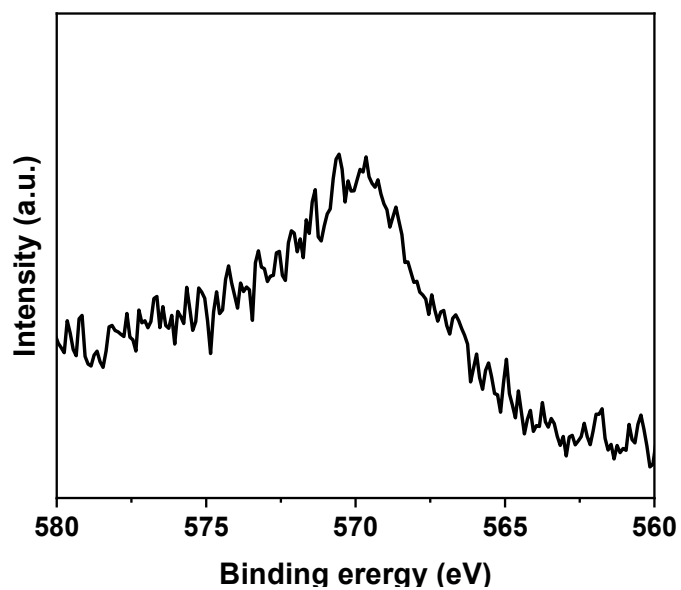
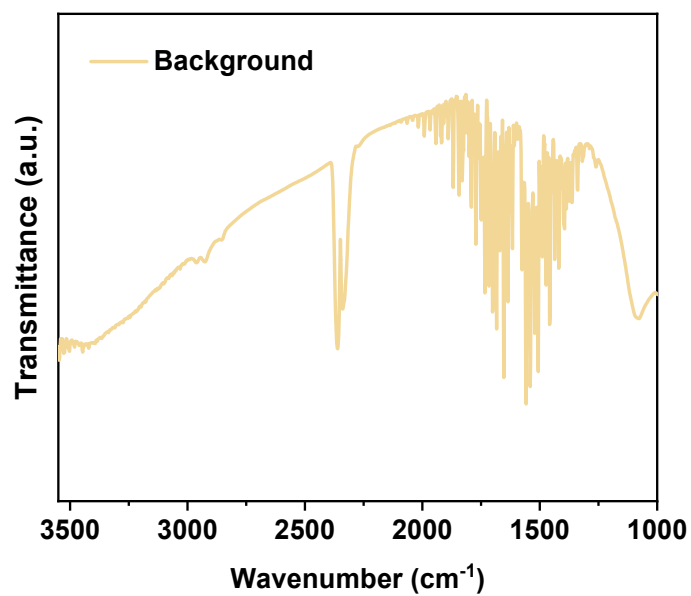


Figure S17. High-resolution Cu 2p XPS spectrum of Cu-HATNA after electrocatalysis.



**Figure S18.** Cu LMM Auger spectrum of Cu-HATNA after electrocatalysis.



**Figure S19.** The background and baseline spectra of ATR-FTIR measurement.

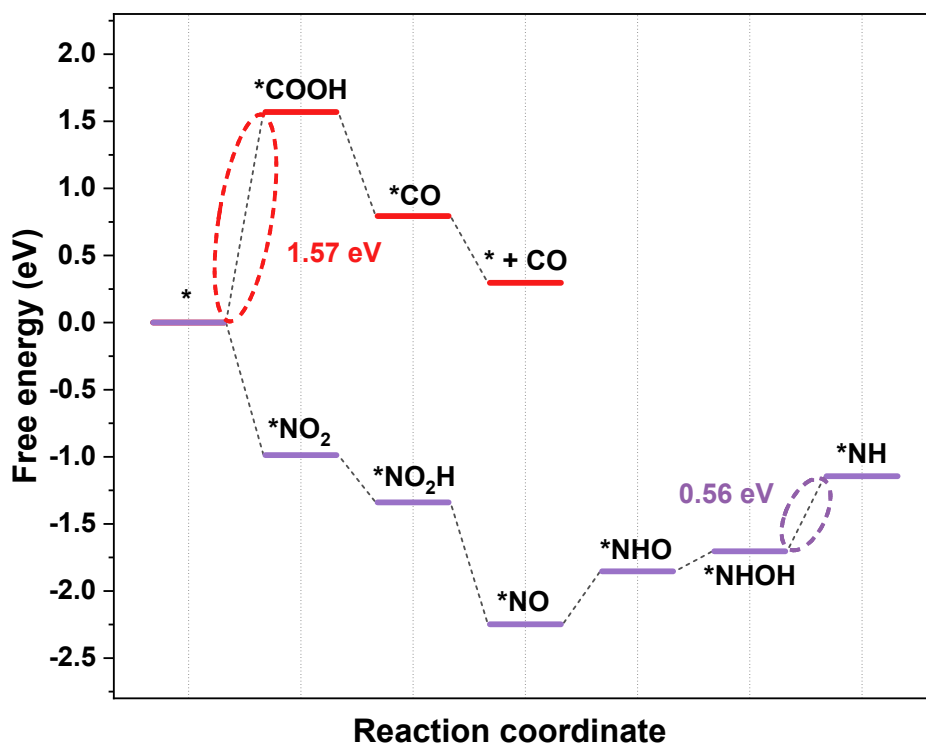


Figure S20. Free energy diagram for CO<sub>2</sub>RR and NO<sub>3</sub>RR on Cu-HATNA.

Table S1. Comparison of electrocatalytic performance of **Cu-HATNA** toward urea synthesis with previously reported catalysts.

Catalyst	Potential (V vs RHE)	FE <sub>urea</sub> (%)	$j_{total}$ (mA cm <sup>-2</sup> )	Yield rate (g h <sup>-1</sup> g <sub>cat</sub> <sup>-1</sup> )	Electrolyte	Ref.
Cu-HATNA	-0.6	25	44.2	1.46	0.1 M KHCO <sub>3</sub> + 0.1 M KNO <sub>3</sub>	<b>This work</b>
In(OH) <sub>3</sub> -S	-0.6	53.4	1	0.55	0.1 M KNO <sub>3</sub>	<i>Nat. Sustain.</i> , 2021, <b>4</b> , 868–876
Vo-InOOH	-0.5	51	2	0.59	0.1 M KNO <sub>3</sub>	<i>ACS Nano</i> , 2022, <b>16</b> , 8213–8222
CuWO <sub>4</sub>	-0.2	70.1 ± 2.4	1	0.1	0.1 M KNO <sub>3</sub>	<i>Nat. Commun.</i> , 2023, <b>14</b> , 4491
MoO <sub>x</sub> -C	-0.6	27.7	4	1.43	0.1 M KNO <sub>3</sub>	<i>Angew. Chem.</i> <i>Int. Ed.</i> , 2023, <b>62</b> , e202301957
Cu-GS-800	-1	25	30	1.8	0.1 M KHCO <sub>3</sub> + 0.1 M KNO <sub>3</sub>	<i>Adv. Energy</i> <i>Mater.</i> , 2022, <b>12</b> , 2201500.
Vo-CeO <sub>2</sub> -750	-1.6	1	45	0.94	0.1 M KHCO <sub>3</sub> + 0.05 M KNO <sub>3</sub>	<i>J. Am. Chem.</i> <i>Soc.</i> , 2022, <b>144</b> , 11530–11535
B-FeNi-DASC	-1.5	17.8	45	1.21	0.1 M KHCO <sub>3</sub> + 0.05 M KNO <sub>3</sub>	<i>Nat. Commun.</i> , 2022, <b>13</b> , 5337
F-CNT	-0.65	18	0.8	0.38	0.1 M KNO <sub>3</sub>	<i>Appl. Catal. B</i> , 2022, <b>316</b> , 121618
Fe(a)@ C-Fe <sub>3</sub> O <sub>4</sub> /CNTs	-0.65	16.5 ± 6.1	5	1.34 ± 0.11	0.1 M KNO <sub>3</sub>	<i>Angew. Chem.</i> <i>Int. Ed.</i> , 2023, <b>135</b> , e202210958
PdCu/CBC	-0.5	59.7 ± 3.4	3	0.76 ± 0.043	0.05 M KNO <sub>3</sub>	<i>EES Catal.</i> , 2023, <b>1</b> , 45–53

Table S2. Cu K-edge EXAFS curve Fitting Parameters.

Sample	Path	CN	$R$ (Å)	$\sigma^2$ ( $10^{-3}$ Å <sup>2</sup> )	$\Delta E_0$ (eV)	$R$ -factor
Cu-HATNA after electrocatalysis	Cu-O	4.28	1.98	2.81	6.07	0.03
Cu-HATNA as synthesised		4.32	1.98	3.15	6.15	0.03

CN, coordination number;  $R$ , distance between absorber and backscatter atoms;  $\sigma^2$ , Debye-Waller factor (a measure of thermal and static disorder in absorber-scatterer distances);  $\Delta E_0$ , threshold Energy Correction ( $|\Delta E_0|$  typically has a value of  $< 10$ ).  $R$ -factor is used to value the goodness of the fitting.

## References

- 1 Y. Liu, S. Li, L. Dai, J. Li, J. Lv, Z. Zhu, A. Yin, P. Li and B. Wang, *Angew. Chem. Int. Ed.*, 2021, **60**, 16409-16415.
- 2 C. Lv, L. Zhong, H. Liu, Z. Fang, C. Yan, M. Chen, Y. Kong, C. Lee, D. Liu, S. Li, J. Liu, L. Song, G. Chen, Q. Yan and G. Yu, *Nat. Sustain.*, 2021, **4**, 868-876.
- 3 P. Giannozzi, S. Baroni, N. Bonini, M. Calandra, R. Car, C. Cavazzoni, D. Ceresoli, G. L. Chiarotti, M. Cococcioni, I. Dabo, A. Dal Corso, S. de Gironcoli, S. Fabris, G. Fratesi, R. Gebauer, U. Gerstmann, C. Gougoussis, A. Kokalj, M. Lazzeri, L. Martin-Samos, N. Marzari, F. Mauri, R. Mazzarello, S. Paolini, A. Pasquarello, L. Paulatto, C. Sbraccia, S. Scandolo, G. Sclauzero, A. P. Seitsonen, A. Smogunov, P. Umari and R. M. Wentzcovitch, *J. Phys.: Condens. Matter*, 2009, **21**, 395502.
- 4 P. Giannozzi, O. Andreussi, T. Brumme, O. Bunau, M. Buongiorno Nardelli, M. Calandra, R. Car, C. Cavazzoni, D. Ceresoli, M. Cococcioni, N. Colonna, I. Carnimeo, A. Dal Corso, S. de Gironcoli, P. Delugas, R. A. DiStasio, A. Ferretti, A. Floris, G. Fratesi, G. Fugallo, R. Gebauer, U. Gerstmann, F. Giustino, T. Gorni, J. Jia, M. Kawamura, H. Y. Ko, A. Kokalj, E. Küçükbenli, M. Lazzeri, M. Marsili, N. Marzari, F. Mauri, N. L. Nguyen, H. V. Nguyen, A. Otero-de-la-Roza, L. Paulatto, S. Poncé, D. Rocca, R. Sabatini, B. Santra, M. Schlipf, A. P. Seitsonen, A. Smogunov, I. Timrov, T. Thonhauser, P. Umari, N. Vast, X. Wu and S. Baroni, *J. Phys.: Condens. Matter*, 2017, **29**, 465901.
- 5 P. E. Blöchl, O. Jepsen and O. K. Andersen, *Phys. Rev. B*, 1994, **49**, 16223-16233.